The Astrophysical Journal Supplement Series, 278:29 (15pp), 2025 May https://doi.org/10.3847/1538-4365/adc0fc

Minute-cadence Observations of the Galactic Plane with the Wide Field Survey Telescope (WFST): Overview, Methodology, and Early Results

Jie Lin[1,2], Tinggui Wang[1,2,3], Minxuan Cai[1,2], Zhen Wan[1,2], Xuzhi Li[4,5], Lulu Fan[1,2,3], Qingfeng Zhu[1,2], Ji-an Jiang[1,2], Ning Jiang[1,2], Xu Kong[1,2,3], Zheyu Lin[1,2], Jiazheng Zhu[1,2], Zhengyan Liu[1,2], Jie Gao[6], Bin Li[7], Feng Li[6], Ming Liang[8], Hao Liu[6], Wei Liu[7], Wentao Luo[3], Jinlong Tang[9], Hairen Wang[7], Jian Wang[6,3], Yongquan Xue[1,2], Dazhi Yao[7], Hongfei Zhang[6], Xiaoling Zhang[7], Wen Zhao[1,2], and Xianzhong Zheng[7]

[1] Department of Astronomy, University of Science and Technology of China, Hefei 230026, People's Republic of China; linjie2019@ustc.edu.cn
[2] School of Astronomy and Space Science, University of Science and Technology of China, Hefei 230026, People's Republic of China
[3] Deep Space Exploration Laboratory, Hefei 230088, People's Republic of China
[4] School of Mathematics and Physics, Anqing Normal University, Anqing 246133, People's Republic of China
[5] Institute of Astronomy and Astrophysics, Anqing Normal University, Anqing 246133, People's Republic of China
[6] State Key Laboratory of Particle Detection and Electronics, University of Science and Technology of China, Hefei 230026, People's Republic of China
[7] Purple Mountain Observatory, Chinese Academy of Sciences, Nanjing 210023, People's Republic of China
[8] National Optical Astronomy Observatory (NSF's National Optical-Infrared Astronomy Research Laboratory), 950 N. Cherry Ave., Tucson, AZ 85726, USA
[9] Institute of Optics and Electronics, Chinese Academy of Sciences, Chengdu 610209, People's Republic of China
Received 2024 December 16; revised 2025 March 13; accepted 2025 March 14; published 2025 May 6

Abstract

As the time-domain survey telescope of the highest survey power in the Northern Hemisphere currently, the Wide Field Survey Telescope (WFST) is scheduled to hourly/daily/semiweekly scan the Northern sky up to ∼23 mag in four optical (*ugri*) bands. Unlike the observation cadences in forthcoming regular survey missions, WFST performed "staring" observations toward the Galactic plane in a cadence of ≈1 minute for a total on-source time of about 13 hr during the commissioning and pilot observation phases. Such an observation cadence is well applied in producing densely sampled light curves and hunting for stars exhibiting fast stellar variabilities. Here we introduce the primary methodologies in detecting variability, periodicity, and stellar flares among half a million sources from the minute-cadence observations, and present the WFST g/r-band light curves generated from periodic variable stars and flaring stars. Benefiting from the high photometric precisions and deep detection limits of WFST, the observations have captured several rare variable stars, such as a variable hot white dwarf (WD) and an ellipsoidal WD binary candidate. By surveying the almost unexplored parameter spaces for variables, WFST will lead to new opportunities in discovering unique variable stars in the Northern sky.

Unified Astronomy Thesaurus concepts: Sky surveys (1464); Optical flares (1166); Short period variable stars (1453)

1. Introduction

Over the last decade, numerous frontier topics on fast stellar variabilities with timescales of minutes to hours have emerged. They involve ultracompact binaries (UCBs; K. B. Burdge et al. 2019, 2020; J. Lin et al. 2024), blue large-amplitude pulsators (BLAPs; P. Pietrukowicz et al. 2017; J. Lin et al. 2023b), rapidly rotating magnetic white dwarfs (WDs; I. Caiazzo et al. 2021; K. A. Williams et al. 2022), transitional cataclysmic variables (CVs; K. B. Burdge et al. 2022a), black widows (K. B. Burdge et al. 2022b), and fast-flaring stars (M. N. Günther et al. 2020; M. Aizawa et al. 2022; W. S. Howard & M. A. MacGregor 2022; Q. Liu et al. 2023). The fast stellar variabilities imply extraordinary physical conditions in pulsation, rotation, orbital motion, or magnetic field for these variable stars, and thus provide crucial windows to study the stellar physics under extreme conditions.

UCBs are a class of binaries with orbital periods shorter than ∼70 minutes. Due to their compact orbits, UCBs avoid harboring a main-sequence (MS) component star (S. Rappaport et al. 1982), and are thus composed of neutron stars (J. Lin & W. Yu 2018; B. Wang et al. 2021), WDs (K. B. Burdge et al. 2020; L. Ren et al. 2023), or hot subdwarfs (S. Geier et al. 2013; T. Kupfer et al. 2020a, 2020b; E. Finch et al. 2023; J. Lin et al. 2024). A part of UCBs are predicted to generate strong gravitational-wave (GW) radiation in millihertz passbands and are thus detectable from space-borne GW detectors, e.g., Tianqin (S.-J. Huang et al. 2020) and the Laser Interferometer Space Antenna (LISA; P. Amaro-Seoane et al. 2017). Since most UCBs are unresolved in GW detectors and their GW signals are superposed incoherently, millions of UCBs in our Galaxy will produce a stochastic foreground signal (i.e., confusion noise; D. Hils et al. 1990; A. J. Ruiter et al. 2010). Fortunately, beyond the confusion noise, space-borne GW detectors will be able to resolve tens of thousands of UCBs (G. Nelemans et al. 2001; A. Lamberts et al. 2019; V. Korol et al. 2022; P. Amaro-Seoane et al. 2023). Nowadays, time-domain survey telescopes are capable of searching for these "verification" UCBs individually from electromagnetic observations in advance, and thus guarantee the operation of GW detectors (T. Kupfer et al. 2018, 2024; E. Finch et al. 2023).

BLAPs represent a rare class of short-period, large-amplitude hot pulsating stars (P. Pietrukowicz et al. 2017). Since BLAPs were first discovered with the Optical Gravitational Lensing Experiment, dozens of BLAPs (or candidates) have been identified successively (T. Kupfer et al. 2019; J. Lin et al. 2022; P. R. McWhirter & M. C. Lam 2022; A. Pigulski et al. 2022;

Table 1
Basic Information for WFST Minute-cadence Observations

Observation	Target	Field Direction	N_{epoch}	Filter	Exposure (s)	Start Time (UTC)	End Time (UTC)
GP-20230918[a]	J0526+5934	05: 26: 10.43 + 59: 34: 45.1	165	*g*	20	2023-09-18 18:20:05	2023-09-18 21:20:29
GP-20231116	J0526+5934	05: 26: 10.43 + 59: 34: 45.1	254	*g*	20	2023-11-16 20:03:47	2023-11-16 23:22:38
GP-20240206[b]	Platais 3	04: 39: 54.24 + 71: 16: 48.0	130	*g*	20	2024-02-06 12:06:36	2024-02-06 15:54:46
GP-20240209	Platais 3	04: 39: 54.24 + 71: 16: 48.0	258	*g*	20	2024-02-09 12:10:52	2024-02-09 15:43:02
GP-20240509	Collinder 350	17: 48: 04.32 + 01: 31: 30.0	176	*r*	30	2024-05-09 17:57:13	2024-05-09 20:45:26

Notes.
[a] Because the operation control system (Z.-y. Zhu et al. 2024) started to work only on 2023 October 30, the observation GP-20230918 was executed manually.
[b] Due to technical tests, GP-20240206 was occasionally interrupted for 73.3 minutes.

J. Borowicz et al. 2023a, 2023b; S.-W. Chang et al. 2024). So far, three candidate stellar models have been proposed for understanding the physical origin of BLAPs: helium-core pre-WDs (A. H. Córsico et al. 2019; C. M. Byrne & C. S. Jeffery 2020; C. M. Byrne et al. 2021), core helium-burning (CHeB) subdwarfs (C. M. Byrne & C. S. Jeffery 2018; T. Wu & Y. Li 2018; X.-C. Meng et al. 2020), and shell helium-burning (SHeB) subdwarfs (H. Xiong et al. 2022; J. Lin et al. 2023b). However, due to deficient and inhomogeneous samples, the physical origin of BLAPs is still controversial. As introduced by J. Lin et al. (2023b), BLAPs may have diverse origins, and the rates of period changes play a crucial role in diagnosing their natures. With the operations of large-aperture survey missions, the growing BLAP samples and their monitoring data will essentially improve the understanding of these mysterious hot pulsating stars.

Stellar flares are dramatically explosive phenomena triggered by impulsive magnetic reconnection in the corona, potentially accompanied by coronal mass ejections (C. Argiroffi et al. 2019), relativistic electron beams (H. A. S. Reid et al. 2014), and chromospheric evaporation (M. Güdel et al. 2002). However, since the typical timescales of optical flares are from minutes to hours, daily/hour-cadence survey missions fail to reproduce temporal flare structures, leading to incorrect estimations for the amplitudes, durations, and energies of flares (H. Yang et al. 2018). Hence, minute-cadence observations, especially as executed by large-aperture, wide-field instruments, will provide rare opportunities to glimpse the flare profiles from dark dwarf stars. In the future, the ultrashort observation cadence (≈0.3 s) of the Tianyu project (F. B. Feng et al. 2024) will even allow us to trace the rapid rise phases of flares and thus help us understand the detailed process of magnetic energy release in dwarf stars.

Aiming at hunting fast stellar variabilities in galaxies, a few wide-field instruments have started performing high-cadence survey missions, e.g., the Zwicky Transient Facility (ZTF; E. C. Bellm et al. 2019; F. J. Masci et al. 2019) high-cadence Galactic plane survey (T. Kupfer et al. 2021), OmegaWhite (S. A. Macfarlane et al. 2015; R. Toma et al. 2016), and the Tsinghua University–Ma Huateng Telescopes for Survey (TMTS; J.-C. Zhang et al. 2020; J. Lin et al. 2022; F. Guo et al. 2024). Benefiting from densely sampled photometry, these missions can well capture fast light variations from diverse variable stars. To investigate rapid stellar variabilities in deep fields, we performed a minute-cadence Galactic plane survey using the Wide Field Survey Telescope (WFST; Z. Lou et al. 2016; T. Wang et al. 2023a), a 2.5 m aperture telescope at Lenghu Observatory with a median seeing of 0.″75 (L. Deng et al. 2021). Equipped with a 6.5 deg^2 field of view and a 0.765 gigapixel mosaic CCD camera (Q. Feng et al. 2024; Z. Geng et al. 2024; H.-f. Zhang et al. 2024), WFST's design enables efficient discovery of transients (Z. Lin et al. 2022; Z.-Y. Liu et al. 2023; S. Huang et al. 2024), variables, and solar system objects (J.-Q. Lu et al. 2025; S.-H. Wang et al. 2025) down to $g, r \approx 23$ mag (L. Lei et al. 2023; Z. Wan et al. 2025). In this paper, we present an overview of the WFST minute-cadence Galactic plane survey executed in its commissioning observation phase (2023 September to 2024 February) and pilot survey phase (2024 March to 2024 June).

2. Observations

Since the commissioning of WFST on 2023 September, we have performed minute-cadence observations of the Galactic plane five times, with a total duration of about 13 hr. As shown in Table 1, these observations were executed uninterruptedly for 3–4 hr, except for the observation GP-20240206, which was occasionally interrupted for 73.3 minutes.[10] With a dead time (caused by overhead) of about 30 s, the observation cadences were ≈50 s and ≈60 s for 20 s exposure and 30 s exposure campaigns, respectively. Notice that, since GP-20230918 was executed manually, the cadence in this observation was nonuniform with an average cadence of about 61 s. All these observations covered three nonoverlapping fields (i.e., J0526 +5934, Platais 3, and Collinder 350), corresponding to a total unrepeated area of ≈20 deg^2. Among them, J0526+5934 and Platais 3 were visited twice for capturing general periodic variable stars,[11] while Collinder 350 was simultaneously observed with both WFST and the Australian Square Kilometre Array Pathfinder (T. Murphy et al. 2013, 2021; Y. Wang et al. 2023b). All these observations were executed using the *g*- or *r*-band filter. The effective wavelengths of the *g*- and *r*-band filters are 476.34 nm and 620.57 nm in theory (L. Lei et al. 2023), respectively, which are similar to those of the Sloan Digital Sky Survey ($\lambda_{eff,SDSS\text{-}g} = 467.18$ nm and $\lambda_{eff,SDSS\text{-}r} = 614.11$ nm; M. Fukugita et al. 1996; D. G. York et al. 2000) but with higher transmittance.

The WFST raw data were primarily dealt with the modified version of the LSST pipeline (M. Jurić et al. 2017), which was developed for the general purpose of photometric data reduction. For single-frame processing, the WFST pipeline (see M. Cai et al. 2025) contains several basic steps. First, the instrumental signatures were removed with the corresponding

[10] Because the interruption time is far shorter than a day, we still refer to GP-20240206 as an uninterrupted observation throughout this paper.
[11] In this work, we refer to variable stars with periods longer than those of typical short-period variable stars as general periodic variable stars, e.g., EW eclipsing binaries and RR Lyrae stars.

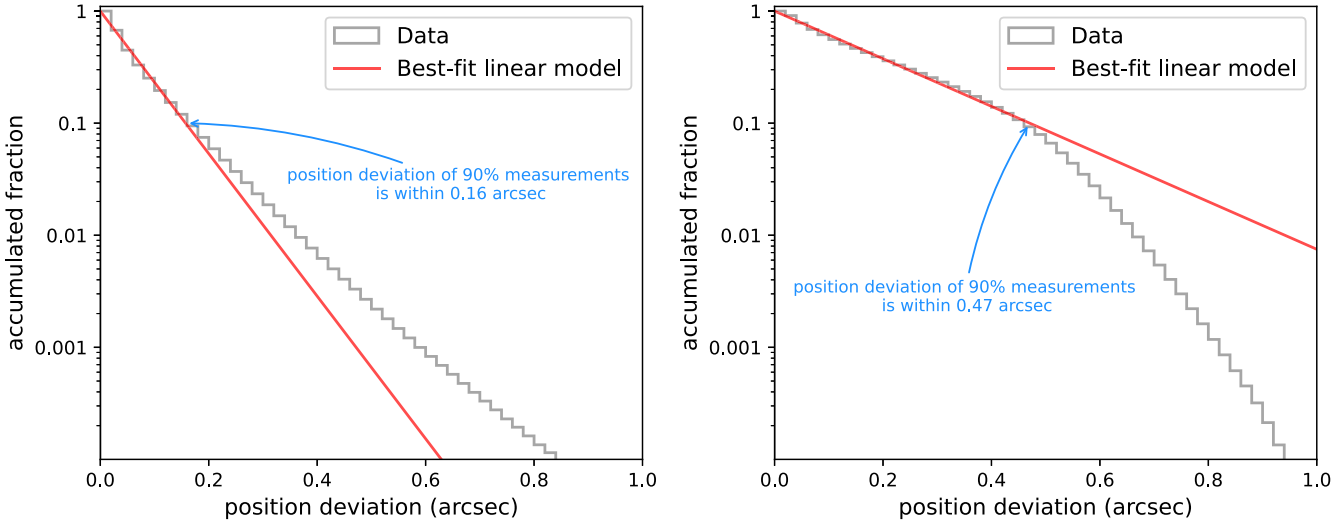

Figure 1. Accumulated fractions for the position deviations from the minute-cadence observations on 2024 February 9. Left: position deviations anchored at average coordinates of the position measurements. Right: position deviations anchored at the coordinates from the first detections of sources. The bin width is 0.″02, and the red lines represent the best-fit linear models for the bins with an accumulated fraction >10%.

calibration exposures, including bias, (sky) flats, fringe, and crosstalk. The instrumental-signature-removed images were then labeled pixel by pixel with blending, saturation, cosmic-ray contamination etc., indicating which part of the images should be ignored or carefully considered in the further analysis. The background was estimated as the median value of each 512 × 512 pixel subregion on the image. A two-dimensional sixth-order Chebyshev polynomial was applied in both the *X*- and *Y*-direction to derive a smooth distribution of the background, and finally produce a background image and a background-subtracted science image. Sources above the detection thresholds were then detected within the background-subtracted science images, and images' point-spread functions (PSFs) were estimated with a selected subsample of the sources. The fluxes of the sources were measured in both different apertures (4.5–70 pixels) and PSF modeling, which were finally calibrated with external references—the astrometric parameters were calibrated to Gaia DR3 (Gaia Collaboration et al. 2016, 2023) and the g/r-band photometric parameters were calibrated to Pan-STARRS DR2 (K. C. Chambers et al. 2016; H. A. Flewelling et al. 2020; E. A. Magnier et al. 2020). Throughout this work, all photometric fluxes were calibrated to AB magnitudes, and the times corresponding to the exposure midpoints were converted into barycentric Modified Julian Dates with barycentric dynamical time ($BMJD_{TDB}$).

All WFST photometric measurements labeled with blending, saturation, cosmic-ray contamination, and image periphery were discarded throughout this work. By crossmatching the photometric measurements within a radius of 1″, we extracted light curves for all sources within the fields. For checking whether the 1″ radius was large enough to bind all photometric measurements from the same sources, we additionally investigated astrometric deviations for all WFST sources with epochs more than 20. The deviations were given by the angular separations between each position measurement and the anchored coordinates, i.e., the average coordinates of the sources here. As shown in the left panel of Figure 1, the accumulated fractions suggest that the astrometric precision of WFST is better than 0.″16 for 90% of the measurements in these early observations. However, since we tend to take the position measurements from first detections as the coordinates of sources, rather than the average ones, a larger radius should be adopted in crossmatching (see the right panel of Figure 1). Here the 1″ radius ensures a ≈0.01% possibility at most that a measurement from a source cannot match its first detection, which effectively prevents splitting a source into multiple sources.

3. Methods

In order to select diverse variables from millions of WFST light curves, we applied three different algorithms in the light-curve analysis (K. V. Sokolovsky et al. 2017), namely algorithms that use the von Neumann ratio η, Osten's method (R. A. Osten et al. 2012), and the Lomb–Scargle periodogram (LSP; N. R. Lomb 1976; J. D. Scargle 1982). Since J. Lin et al. (2022) have detailed how these algorithms work on uninterrupted light curves obtained from minute-cadence survey observations, here we introduce only the basic principles for these algorithms and their performance for WFST observation data. Furthermore, we also crossmatch the WFST sources with the Gaia DR3 catalog (Gaia Collaboration et al. 2016, 2023) for locating them in the color–magnitude diagram (CMD), which plays a crucial role in preliminary identifications of variable stars.

3.1. Variability Detection

In order to test the variability detection in the observation data, we extracted light curves (with ⩾20 epochs) from *g*-band observation GP-20240209 and *r*-band observation GP-20240509. Among them, GP-20240209 contributed 119,119 uninterrupted light curves, while GP-20240509 provided 262,628 ones. The statistical characteristics for these light curves are presented in Figure 2. In the *g*-band observations, the WFST light curves are distributed predominantly from 12.9 to 22.3 mag, and the number of light curves increases along with the median magnitude and peaks around 22 mag. Under suboptimal observation conditions (see Table 2), the median magnitudes of the *r*-band light curves here range from 12.2 to 20.6 mag. Notice that varying source detection thresholds were implemented in different observation phases: 3σ above the background noise for GP-20231116, GP-20240206, and GP-

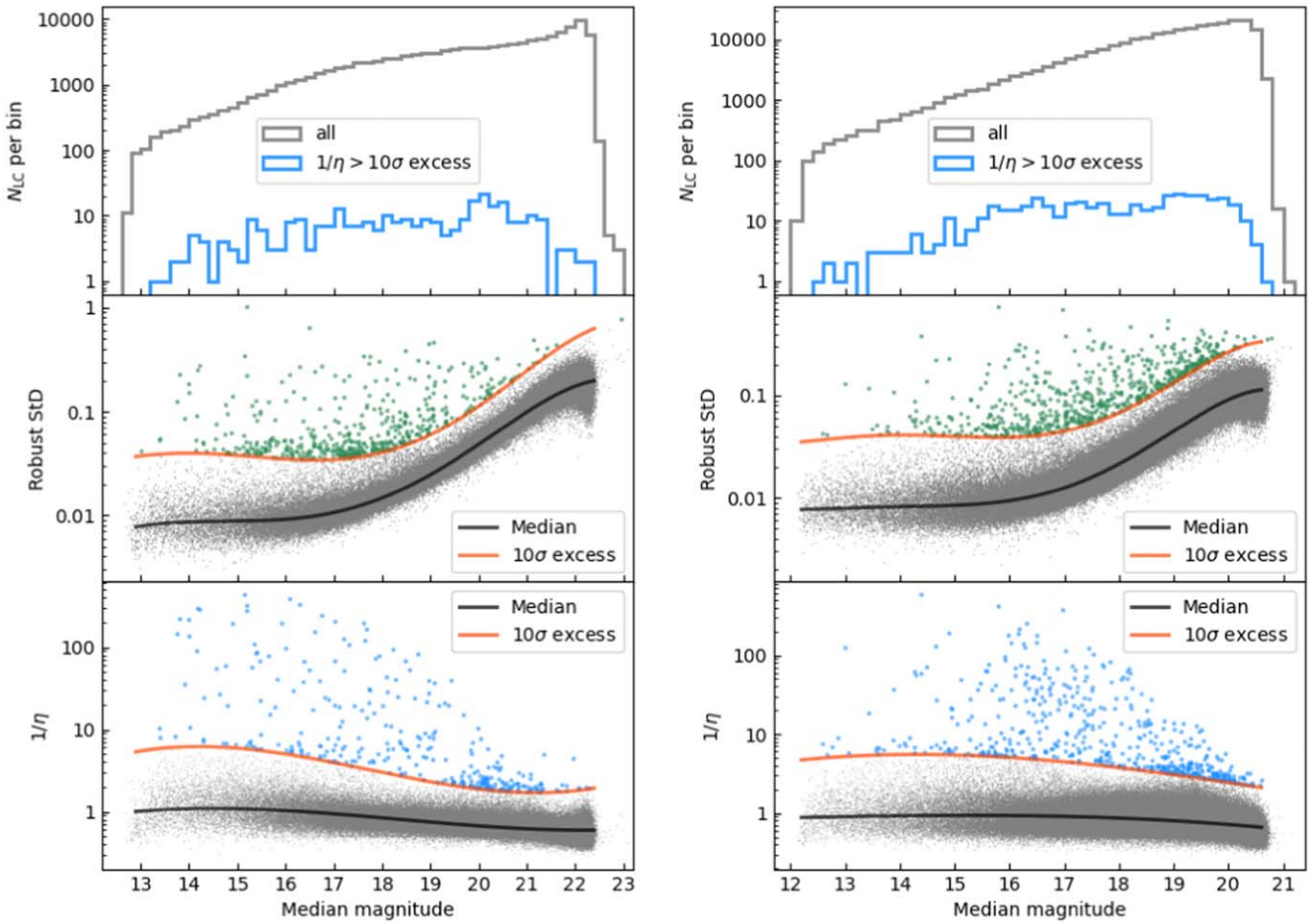

Figure 2. Distributions for number (upper), robust standard deviation (middle), and inverse von Neumann ratio (lower) against the median AB magnitude, derived from the light curves extracted from g-band observation GP-20240209 (left) and r-band observation GP-20240509 (right). Upper panels: the gray lines represent the number of light curves (with $\geqslant$20 epochs) per bin, while the blue lines represent the number of candidate variable stars (with $1/\eta$ above the 10σ threshold) per bin. The bin size is 0.2 mag. Middle panels and lower panels: the black and red lines represent the medians and 10σ excesses for the distributions of variability indices, respectively. The gray and green/blue points represent the light curves with variability indices below and above the 10σ thresholds, respectively.

20240209, versus 5σ for GP-20230918, GP-20240509, and subsequent observations. While the stringent threshold excludes marginally detectable faint sources, it effectively suppresses artificial detections from observations.

Similar to the standard deviation (StD), the robust StD is a variability index quantifying the scatter of brightness measurements based on the 25th percentile of measurements above/below the median. Because only the inner 50th percentile of measurements are used to derive the StD (see also E. O. Ofek et al. 2020), the robust StD is immune from outliers or occasional real variations (e.g., fast flares). As shown in the middle panels of Figure 2, the robust StD rises from 0.008 mag to $\sim$0.2 mag with the darkening of sources, while the variation trend represents the photometric precisions at various magnitudes. Based on the robust StDs binned at various magnitudes, the statistical information for the WFST minute-cadence observations is summarized in Table 2.

Light curves that present significantly larger scatters than the expected uncertainties are likely generated from variable sources. By fitting the 10σ excesses at various magnitudes with fifth-order polynomial models, 462 and 634 candidate variable sources were selected from GP-20240209 and GP-20240509, respectively, implying about three candidate variables per 1000 observed sources. However, due to blending, saturation, stray lights, and varying atmospheric extinction with the altitude, the candidate variable sources inevitably include a large proportion of nonastrophysically variable sources.[12] As T. Kupfer et al. (2021) introduced, about 60%–85% of candidate variable sources present spurious variations from the ZTF high-cadence observations, especially in crowded fields; J. Lin et al. (2022) also revealed a false-positive rate[13] of 67% from their 10σ-excess variable candidates in the first-year minute-cadence observations of TMTS. By visually checking the WFST light curves from all candidate variable sources, we found that the false-positive rate is 76% for GP-20240209 and 65% for GP-20240509. However, because the robust StD is extremely insensitive to temporary light variations in the light curves, we tended to adopt another variability index to detect the brightness variability of sources including flaring stars.

After comparing 18 variability indices that quantify scatter and/or correlation among photometric time series, K. V. Sokolovsky et al. (2017) concluded that the von Neumann ratio η (or the inverse von Neumann ratio $1/\eta$, conventionally) is one of the best indices in selecting candidate variables. The von Neumann ratio can test the independence of successive

[12] Sources with light variations that are not caused by real astrophysical variability.

[13] The ratio of nonastrophysically variable sources to all candidate variable sources here.

Table 2
Statistical Information for WFST Minute-cadence Observations

Observation	Average FWHM[a] (arcseconds)	Photometric Precision[b] (mag)			Limiting Magnitude[c] (mag)		Number of Sources	
		15 mag	18 mag	20 mag	5σ	10σ	20 Epochs	50 Epochs
GP-20230918	2.00	0.0057	0.0138	0.0547	…[d]	20.859	76,517	60,635
GP-20231116	1.81	0.0124	0.0181	0.0604	21.786	20.716	115,637	95,847
GP-20240206	2.51	0.0082	0.0196	0.0825	21.371	20.300	76,773	57,436
GP-20240209	1.67	0.0088	0.0147	0.0480	22.338	21.071	119,199	98,475
GP-20240509	2.40	0.0084	0.0214	0.0909	…[d]	20.267	262,628	219,339

Notes.
[a] The average full widths at half-maximum (FWHMs) are determined by the PSFs of field sources, which characterize the observation conditions.
[b] Photometric precision values are calculated by averaging robust standard deviations (StDs) binned at 15, 18, and 20 mag.
[c] Limiting magnitudes are defined as the median magnitudes at robust StD = 0.2 mag (5σ level) and 0.1 mag (10σ level). Notice that the minute-cadence observations are confined to a single night and a localized sky region; consequently, the derived limiting magnitudes here are not representative of WFST's full capabilities.
[d] The implementation of a stringent 5σ detection threshold (see Section 3.1) inherently precludes determination of the 5σ limiting magnitudes through quantification of the photometric scatter, as faint sources below the threshold are systematically excluded from the analysis.

brightness measurements, and is thus applied in variability detection for light curves affected by outliers. The inverse ratio $1/\eta$ can be calculated by

$$\frac{1}{\eta} = \frac{\sum_{i=1}^{N}(m_i - \overline{m})^2}{\sum_{i=1}^{N-1}(m_{i+1} - m_i)^2}, \quad (1)$$

where m_i and m_{i+1} represent the ith and $(i+1)$th magnitudes in the light curve, respectively; $\overline{m}$ is the average magnitude over all epochs; and N denotes the number of epochs. The inverse ratio $1/\eta$ is expected to be 0.5 for an ideal time series following a Gaussian distribution. However, due to astrophysical variations and various photometric issues, the distributions of real photometric measurements actually deviate from Gaussian distributions. As shown in the lower panels of Figure 2, $1/\eta$ decreases from $\sim$1 to 0.6 along with the magnitude. Similarly, we fitted the 10σ excesses against the median magnitudes using third-order polynomial models, which led to 306 and 527 candidate variable sources selected from GP-20240209 and from GP-20240509, respectively. These candidate variable sources include a dozen flaring stars that were missed in the selections based on the robust StD. By visually checking the light curves, we found that the false-positive rate drops to 60% for GP-20240209 and to 53% for GP-20240509, implying that the von Neumann ratio is a much better variability index to select variable stars. As both r- and g-band minute-cadence observations suggest that about 0.1% of observed sources exhibit real astrophysical variability, WFST is expected to reveal several million variable sources among five billion significantly detected sources within the Galaxy in the future (T. Wang et al. 2023a).

Furthermore, in order to search for specific types of variable stars, we prefer to use Osten's method and the LSP to select flaring stars and periodic variable stars, respectively, while the variability indices are used as an auxiliary tool to improve the completeness of selections.

3.2. Flare Detection

In order to search for fast flares in minute/hour timescales from minute-cadence observation data, we applied the flare selection method described in R. A. Osten et al. (2012) and the false-discovery rate (FDR) analysis used by J. Lin et al. (2022). Before the selections, all 531,732 uninterrupted light curves (with epochs $\geqslant 50$) were detrended using a compound model of a fourth-order Fourier series and a second-order polynomial (see Equation (7) in J. Lin et al. 2022). Given the hour-level observation spans, the polynomial components here are intended for offsetting potential long-timescale variations induced by both astrophysical (e.g., long-period eclipsing binaries) and nonastrophysical (e.g., varied altitude angles) factors.

For obeying the normal distribution, the detrended magnitudes ($m_{\rm dtr} = m - m_{\rm model}$) are normalized as

$$V_i = \frac{\overline{m_{\rm dtr}} - m_{{\rm dtr},i}}{\sigma_{\rm dtr}}, \quad (2)$$

where $m_{{\rm dtr},i}$ represents the ith detrended magnitude, and $\overline{m_{\rm dtr}}$ and $\sigma_{\rm dtr}$ represent the median and robust StD of the detrended magnitudes, respectively.

Following the approach introduced by R. A. Osten et al. (2012), flares in the light curves could be detected through at least two consecutive positive outliers in the time series. The index quantifying the significance of two consecutive outliers in a time series is defined as the product of continuous two normalized detrended magnitudes, namely

$$\phi_{{\rm V\,V},i} = V_i \times V_{i+1}. \quad (3)$$

For the purpose of selecting flares (rather than dips or eclipses), the adopted $\phi_{{\rm V\,V},i}$ pairs require both $V_i > 0$ and $V_{i+1} > 0$. To simplify calculations, only the maximum $\phi_{{\rm V\,V},i}$ over a time series (i.e., $\phi_{{\rm V\,V,max}} = \max_i\{\phi_{{\rm V\,V},i} \mid_{V_i>0, V_{i+1}>0}\}$) is applied to the flare detection. In other words, a light curve having a higher $\phi_{{\rm V\,V,max}}$ is more likely to present flares.

Benefiting from the probability density function for $\phi_{\rm V\,V}$ given by J. Lin et al. (2022), we can calculate the FDRs of flares in theory for WFST light curves via

$${\rm FDR} = 1 - \left[1 - \frac{1}{2\pi}\int_{\phi_{\rm VV,max}}^{\infty} K_0(|x|)\, d\, x\right]^{N-1}, \quad (4)$$

where K_0 represents the special $(n=0)$ case of a modified Bessel function of the second kind (M. Abramowitz & I. A. Stegun 1972), and $N-1$ is the number of $\phi_{\rm V\,V}$ for a

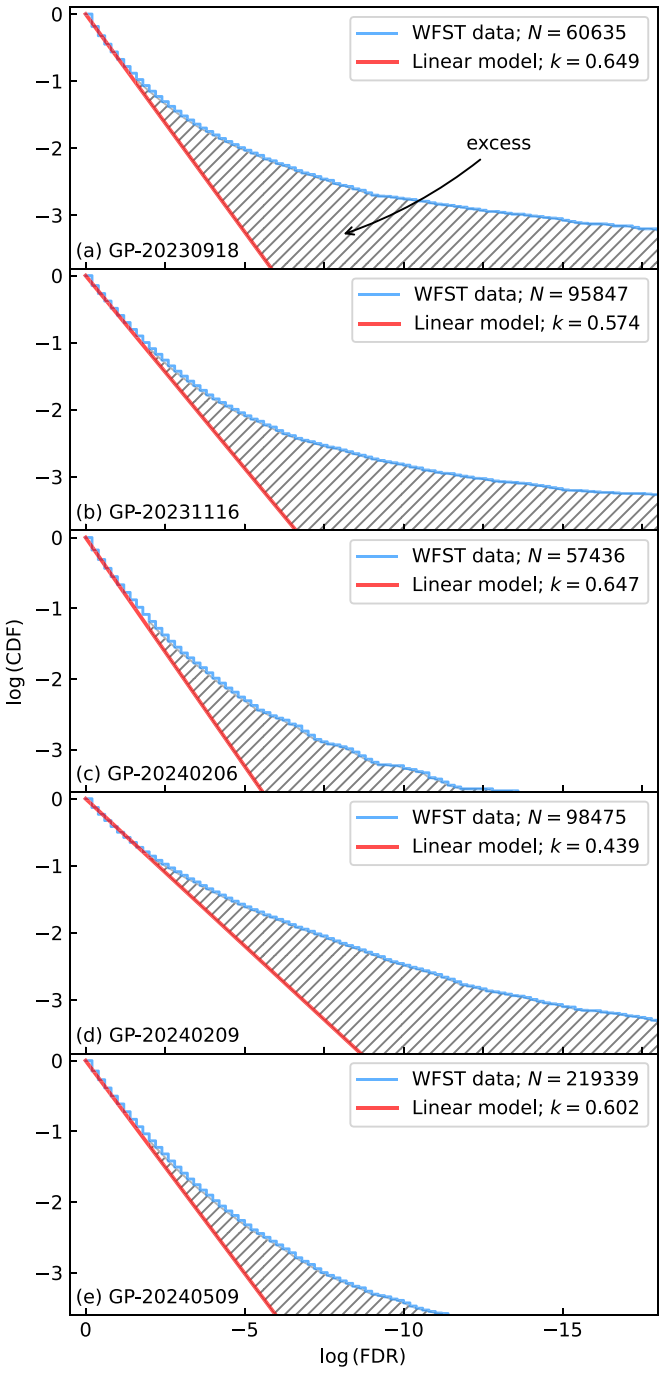

Figure 3. CDFs of FDRs for flare detection from WFST minute-cadence observations. The FDR histograms (blue solid lines) in panels (a)–(e) are $\phi_{\mathrm{V\,V}}$ sequences derived from five WFST minute-cadence observations. And the red solid lines are the best-fit linear models for the histogram bins at $\log(\mathrm{CDF}) \geqslant -1$. The bin size is 0.2. The hatched areas indicate that the observed FDR distributions exceed the models.

time series of N epochs. The cumulative distribution functions (CDFs) of these FDRs are shown in Figure 3. Given the prerequisite that only a small fraction of light curves exhibit flares, we fitted the histogram bins at $\log(\mathrm{CDF}) \geqslant -1$ (i.e., the cumulative distributions for 90% of the light curves) with a linear model, $\log(\mathrm{CDF}) = k \times \log(\mathrm{FDR})$. Since the magnitudes in light curves do not tightly follow Gaussian distributions and are not completely independent of each other, it is common for the cumulative distributions of FDRs to deviate from the ideal null distribution (i.e., CDF = FDR; see also J. Lin et al. 2022). By regarding the best-fit models as the null distributions, FDRs can be calibrated via the best-fit slope k, namely $\mathrm{FDR_{cal}} = \mathrm{FDR}^{k}$. Given the nonastrophysical outliers induced by potential issues (e.g., bleeding of saturated sources) in early observation data, we adopted a tight threshold for false-detection rates (i.e., $\mathrm{FDR_{cal}} \leqslant 10^{-6}$), leading to 486 flaring star candidates selected from the light curves. By visually checking all candidates, we found that 33 present real flares, while most of the artificial flares are caused by the bleeding of saturated sources or by incorrect models for detrending. Nonetheless, the number of flaring stars revealed from the total of 15 hr of WFST observations is comparable to the number of all flaring stars discovered among the first-year TMTS observations (J. Lin et al. 2022; Q. Liu et al. 2023).

However, since the observation spans are only 3–4 hr, Osten's method failed to model the quiescence fluxes for the "long-duration" flares lasting for $\gtrsim$1 hr, leading to the omission of these "energetic" flares from the selections above. Given that "energetic" flares must exhibit significantly strong variability, we visually checked the variable star candidates with high $1/\eta$ values and picked out four additional flares. These "energetic" flares having diverse light-curve morphologies are presented in the following section.

3.3. Periodicity Detection

The LSP (N. R. Lomb 1976; J. D. Scargle 1982) is a common tool to reveal periodic variation signals from unevenly sampled time series. In order to reveal both short-period variable stars and general periodic variable stars, the LSPs for the WFST light curves were calculated under two different sets.

3.3.1. Short-period Variable Stars

Aiming at searching for short-period variable stars, we calculated variance-scaled LSPs (see Equation (1) of M. W. Coughlin et al. 2021 or Equation (5) of J. Lin et al. 2022) for all uninterrupted light curves with epochs $\geqslant$50 within the frequency range of $2/T$ to f_{nyq}, where T represents the time spans of the uninterrupted observations and f_{nyq} is the (pseudo-) Nyquist frequency (J. T. VanderPlas 2018). The f_{nyq} here was set to half of the average sampling rate f_0, i.e., $1/100$ Hz for the 20 s exposures and $1/120$ Hz for the 30 s exposures. Due to the limitation from the lowest frequency $2/T$, these LSPs can only be used to detect variable stars with a period shorter than 1.5–2 hr.

The false-alarm probability (FAP), which quantifies the significance of a periodic signal, is generally inferred from the maximum power ($\mathrm{Pwr_{max}}$) over an LSP (e.g., Equation (54) of J. T. VanderPlas 2018). However, for the uninterrupted light curves obtained within single nights, the distributions of $\mathrm{Pwr_{max}}$ are severely affected by window functions and are thus frequency-dependent. To avoid missing short-period variable sources, J. Lin et al. (2023a) suggested that the $\mathrm{Pwr_{max}}$–f_{max} diagram should be applied in the periodicity detection for single-night observations, where f_{max} is the frequency corresponding to the maximum power $\mathrm{Pwr_{max}}$ within an LSP. As shown in Figure 4, f_{max} distributes over the investigated frequency ranges, while $\mathrm{Pwr_{max}}$ integrally tends to much higher values at the low-frequency ends. As the targeted star in both GP-20230918 and

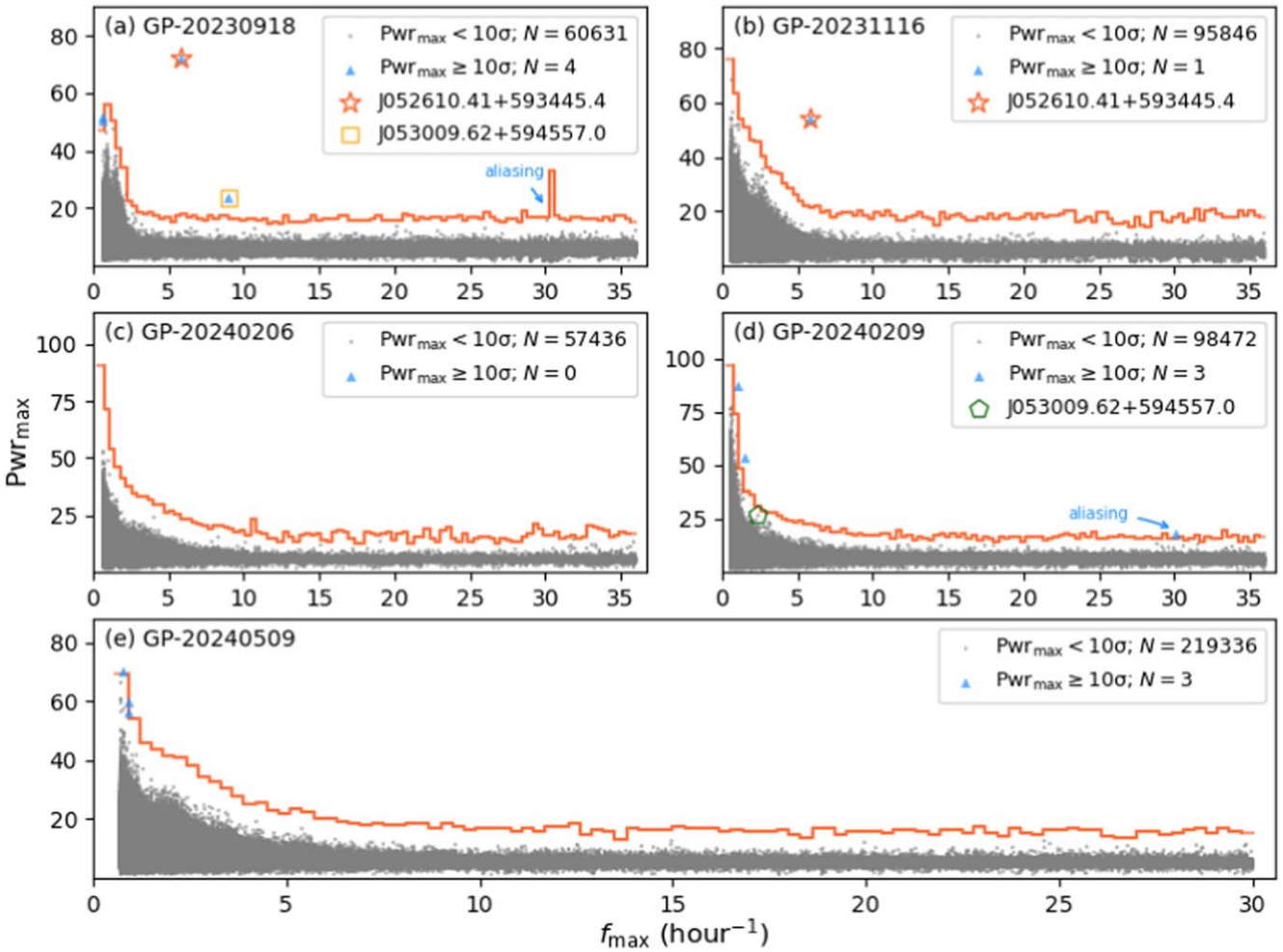

Figure 4. Distributions of maximum power Pwr_{max} vs. the corresponding frequency f_{max}. Data points in panels (a)–(e) are LSPs derived from five WFST minute-cadence observations. The red solid line represents 10σ excesses, and the total numbers (N) of sources above/below the 10σ threshold are indicated in the legends. Several interesting short-period objects are highlighted with hollow symbols.

GP-20231116, the periodicity of J0526+5934 (highlighted in panels (a) and (b) of Figure 4; see also A. Kosakowski et al. 2023; J. Lin et al. 2024; A. Rebassa-Mansergas et al. 2024) is well reproduced in WFST observations. Thanks to lower "noise" at higher frequency in the Pwr_{max}–f_{max} diagram, a 6.7 minute variable star J053009.62+594557.0 (R.A. $\alpha = 82.5401$ and decl. $\delta = 59.7661$, hereafter J0530+5945, highlighted in panel (a) of Figure 4) emerges out of 60,000 candidate sources.

In order to pick out periodic variable source candidates with frequency-dependent thresholds, each Pwr_{max}–f_{max} diagram was divided into 100 uniform frequency intervals, and each frequency bin independently derives the thresholds corresponding to 10σ excesses. Given the thresholds, 10 (unrepeated) periodic variable source candidates were selected. By visually checking all these candidates, we found nine (out of 10) exhibit real periodicity, while only one candidate is induced by aliasing periodic signals of around 2 minutes. We tried to lower the selection threshold in order to include more candidates. However, the weak periodicity from these additional candidates was very difficult to identify and confirm. Nonetheless, we highlighted an interesting periodic variable star (i.e., J0530+5945) below the 10σ excesses from the observation GP-20240209 (see panel (d) of Figure 4). We will present further classifications for these short-period objects through the CMD in Section 4.

3.3.2. General Periodic Variable Stars

In order to mine and present diverse periodic variable stars from our minute-cadence observations, we spliced the uninterrupted observations having consistent pointings, i.e., GP-20230918+GP-20231116 (SO1 hereafter) and GP-20240206 +GP-20240209 (SO2 hereafter). Since the observation spans are greatly extended to about 3 months/3 days for SO1/SO2, the splicing light curves are thought to be used for detecting periodic variable stars longer than tens of hours. However, due to the observation strategy developed for capturing short-period variable stars, the splicing observations actually cover minor, nonuniform phase ranges of those potential long-period variable stars. Owing to an extremely uneven sampling cadence, their window functions are dramatically amplified below the frequency of about $3\,\mathrm{day}^{-1}$. Hence, we calculated the variance-scaled LSPs for all splicing light curves with epochs $\geqslant 50$ within a fixed frequency range, $3\,\mathrm{day}^{-1}$ to $12\,\mathrm{day}^{-1}$.

The FAPs were obtained following the independent frequency method (J. T. VanderPlas 2018), namely

$$\mathrm{FAP} = 1 - [1 - \exp(-\mathrm{Pwr}_{max})]^{N_{\mathrm{eff}}}, \quad (5)$$

where N_{eff} is the effective number of independent frequencies, which is assumed to be the investigated frequency range in units of expected frequency width ($\delta f = 1/T$). As Figure 5 shows, due

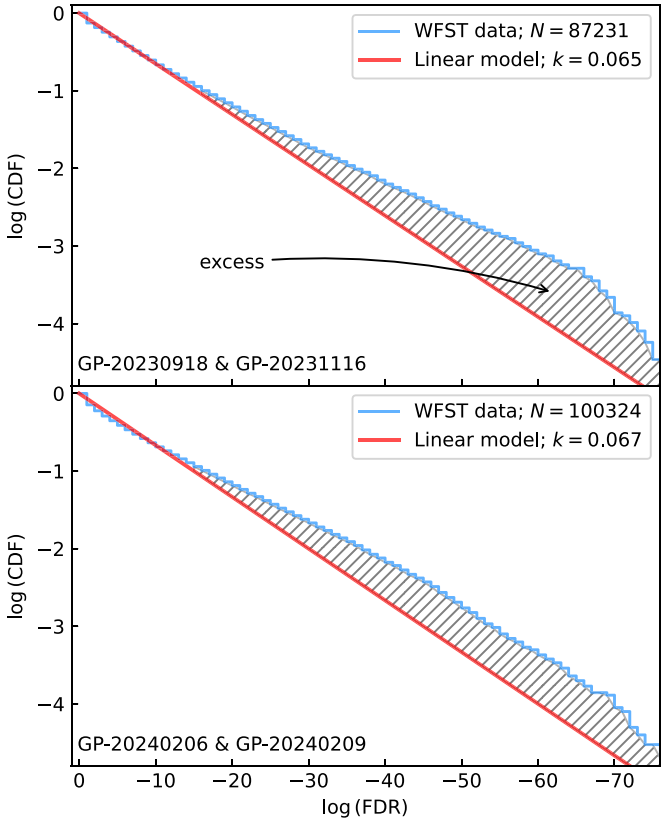

Figure 5. CDFs of FAPs for periodicity detection from the splicing observations. The data sets were obtained from GP-20230918+GP-20231116 (upper) and GP-20240206+GP-20240209 (lower). The blue lines represent the CDFs derived from WFST observation data, and the red lines are the best-fit linear models for the bins with log(CDF) $\geqslant -1$. The bin size is 1.0.

to the systematic overestimation of $\mathrm{Pwr}_{\mathrm{max}}$ induced by window functions, the cumulative distributions of FAPs deviate considerably from the ideal null distribution. In order to reproduce the null distributions for the observation data, we tried to fit the histogram bins at $\log(\mathrm{CDF}) \geqslant -1$ with $\log(\mathrm{CDF}) = k \times \log(\mathrm{FAP})$. Similar to the approach for flare searches, the FAPs were calibrated by $\mathrm{FAP}_{\mathrm{cal}} = \mathrm{FAP}^{k}$ based on the best-fit linear models. By adopting an FAP threshold of 0.1%, 288 and 374 candidates were selected from SO1 and SO2, respectively. Among them, we visually confirmed 146 variable stars having real periodic variations. Notice that the 3 hr uninterrupted observations are not intended to serve the search of variables in such light variation periods. Here the mining of periodic variable stars from splicing observations is made in an effort to present plentiful types of variable stars in the early results of WFST.

3.4. Crossmatch with Gaia DR3 Catalog

Besides selections based on diverse light variations, the additional photometric and astrometric information provided by external catalogs is effective for filtering and identifying variable stars. Since the CMD plays a crucial role in the classification of short-period variable stars (J. Lin et al. 2023a), we crossmatched all 500,460 WFST sources (corresponding to 650,696 uninterrupted light curves having epochs $\geqslant 20$) with Gaia DR3 sources (Gaia Collaboration et al. 2023) within $2''$. As a result, 489,801 WFST sources (97.87%) match at least a Gaia counterpart. Among them, 102,509 (20.93%) Gaia sources have a reliable parallax measurement (i.e., $\varpi/\sigma_{\varpi} \geqslant 5.0$), which allows us to calculate absolute magnitudes and estimate interstellar dust extinctions.

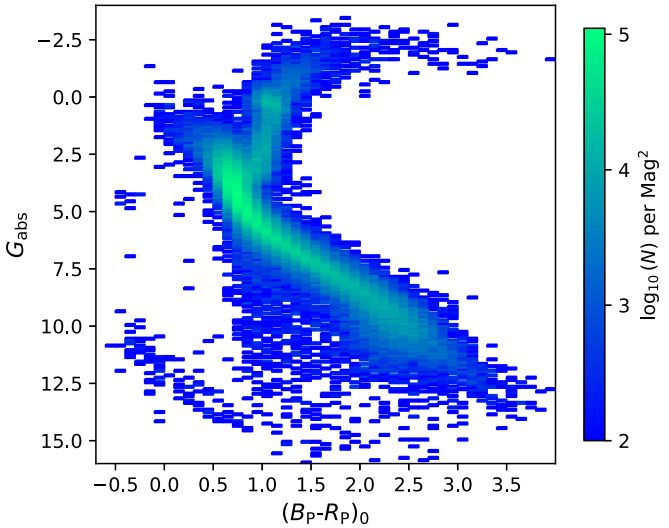

Figure 6. Density distribution of the Gaia DR3–WFST sources across the CMD. Only the Gaia DR3 sources having a reliable parallax measurement are included in the distribution. Both magnitudes and colors are calibrated for interstellar dust extinction and reddening. The bin size is 0.1×0.1 mag^2.

We present the density distribution for 100,000 Gaia DR3–WFST sources in the CMD (Figure 6). Both magnitudes and colors are already calibrated for interstellar dust extinction and reddening, which are obtained from a three-dimensional dust map (G. M. Green et al. 2019) with the DUSTMAPS Python package[14] (G. M. Green 2018). As Figure 6 shows, the Gaia DR3–WFST sources cover diverse regions over the CMD, including the main sequence, red giant branch, extreme horizontal branch, and WD cooling sequence. Aiming at searching for UCBs harboring double WDs, all WFST sources were also crossmatched with the catalog of WDs in Gaia EDR3 (N. P. Gentile Fusillo et al. 2021), leading to 263 WD candidates identified from the WFST sources. Benefiting from the large aperture and thus high detection depth, the number of WDs covered by three pointings of WFST is comparable with the number covered by 90 TMTS fields (J. Lin et al. 2022).

4. Early Results

Following the methods introduced in the previous section, we present selected periodic variable stars and flaring stars across the CMD (Figure 7). The periodic variable stars occupy the zones of A-, F-, and G-type MS stars while the flaring stars are concentrated on the late-type main sequence. In this section, we will show WFST performance in detecting variable stars, and introduce several interesting objects in detail.

4.1. General Periodic Variable Stars

Among the 146 selected general periodic variable stars in Section 3.3.2, 118 objects were already identified by the International Variable Star Index (VSX; C. L. Watson et al. 2006). According to the variable star types provided by VSX, 89% of these objects are identified as EW-type eclipsing binaries and 6% are RR Lyrae variables. Notice that, since the typical

[14] https://github.com/gregreen/dustmaps

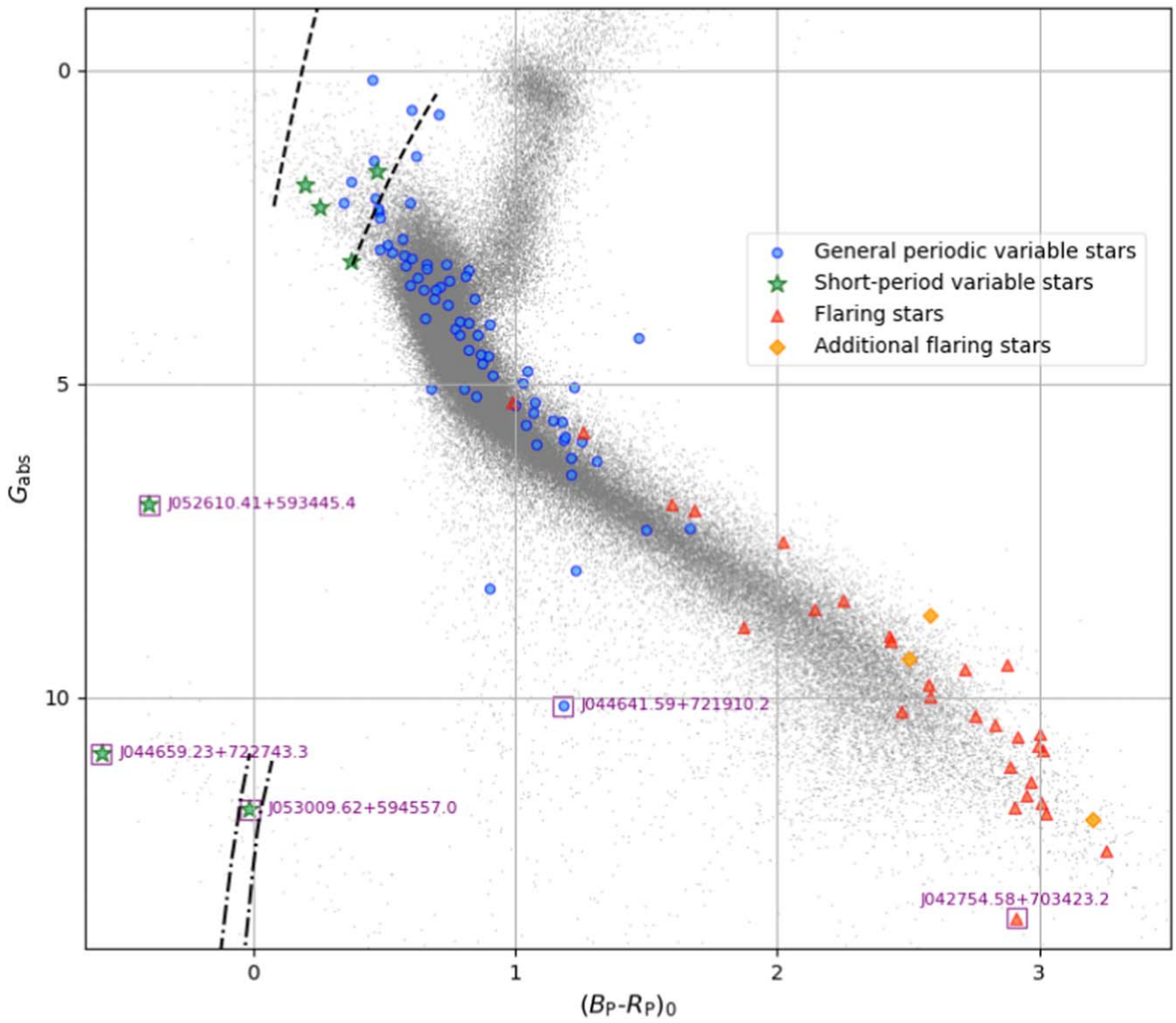

Figure 7. Distributions of periodic variable stars and flaring stars across the CMD. The general periodic variable stars, short-period variable stars, and flaring stars were selected by the three different methods introduced in Section 3. The additional flaring stars were discovered by visually checking the variable star candidates with high $1/\eta$ values rather than by Osten's method. Several interesting objects are highlighted by purple squares. The gray dots in the background are the sources detected from the 15 hr WFST observations. We denote the instability strip edges of δ Sct (S. J. Murphy et al. 2019) and ZZ Cet (I. Caiazzo et al. 2021) with dashed lines and dotted–dashed lines, respectively.

pulsation period of fundamental-mode (RRab) Lyrae is 0.3–1.0 day, which exceeds the investigated frequency range (i.e., 3 day^{-1} to 12 day^{-1}) of our LSPs, these pulsators are occasionally revealed when the LSPs capture their high-frequency harmonics. Figure 8 presents phase-folded light curves for several general periodic variable stars within diverse magnitude ranges. The photometry with high signal-to-noise ratio allows WFST to independently discover eclipsing binaries and pulsating stars from 14 mag to darker than 20.5 mag. Owing to our observation strategy aiming at searching for short-period variable stars, the phases of these "long-period" objects are incompletely covered by our observations. With the coming of regular surveys, we will systematically introduce WFST's detection capability for periodic variable stars in the future.

A newly discovered ellipsoidal binary (candidate) containing a WD and a low-mass MS star. Among the selected general periodic variable stars, a sample is found to deviate significantly from the main sequence in the CMD (Figure 7), namely WFST J044641.59+721910.2 ($\alpha = 71.6733$ and $\delta = 72.3195$, hereafter J0446+7219). Its periodicity and sinusoidal-like light-curve profile are double-checked by ZTF observations (see Figure 9). J0446+7219 [$G_{abs} = 10.13$ mag and $(B_P - R_P)_0 = 1.18$] locates in a CMD region corresponding to magnetic CVs (J. Lin et al. 2023a) or WD–MS binaries (A. Rebassa-Mansergas et al. 2021). Due to the fact that magnetic CVs rarely exhibit sinusoidal-like light curves (see also Q. Liu et al. 2024), we are inclined to support the observation that J0446+7219 is an ellipsoidal binary with an orbital period of 5.90 hr in which a low-mass MS star is tidally deformed by its WD companion. The spectroscopic identifications on Balmer lines and TiO bands could provide further evidences to support/refute the inference.

4.2. Short-period Variable Stars

As introduced in Section 3.3.1, 10 short-period variable stars were selected from the Pwr_{max}–f_{max} diagrams. As the dominant "noise" sources in systematic searches of interesting short-period

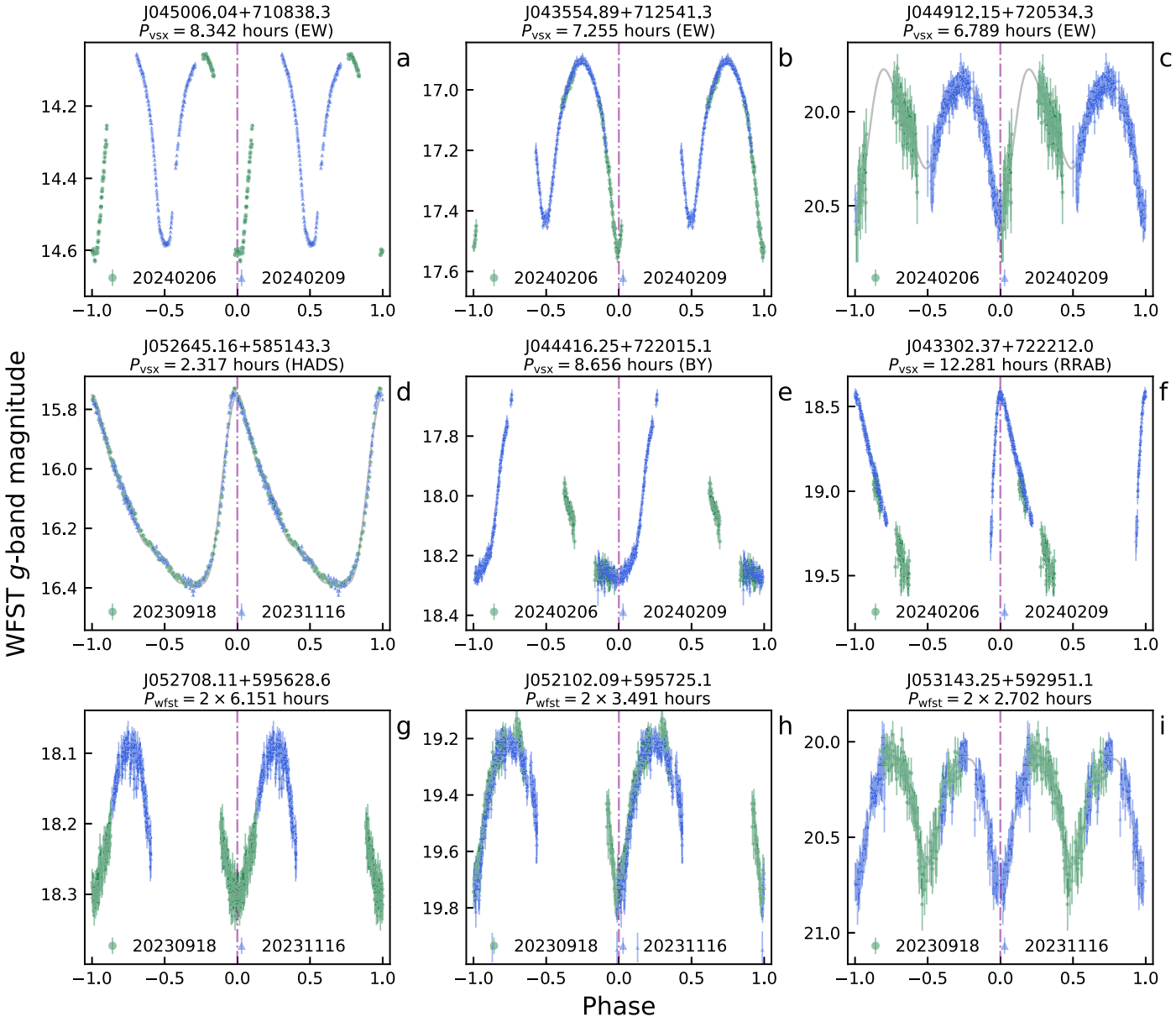

Figure 8. A gallery of phase-folded light curves for nine general periodic variable stars revealed by the splicing observations. All light curves are obtained from the *g*-band observations of WFST, and the exposure is 20 s. For the objects identified by VSX, their light curves (panels (a)–(f)) are folded by the period provided by VSX; for the variables first identified by WFST, the light curves (panels (g)–(i)) are folded using twice the photometric periods (i.e., $1/f_{max}$) obtained from the WFST LSPs. We label the classification type for the objects identified by VSX: EW = EW-type eclipsing binary, HADS = high-amplitude δ Sct star, RRAB = RRab Lyrae, and BY = BY Dra–type variable. The light curves having relatively complete phase coverage (i.e., panels (c), (d), and (i)) are modeled using a fourth-order Fourier series (the gray solid lines).

variable stars (J. Lin et al. 2023a), hour-period δ Sct stars are the main variable stars in our samples (e.g., the green stars within the classical instability strip of Figure 7). We present an example of a δ Sct star detected by WFST in panels (a) and (e) of Figure 10. With the increment in detection depths of survey telescopes, a large number of distant δ Sct stars discovered by new instruments will have no credible parallax measurements from Gaia. Hence, an identification tool that can distinguish δ Sct stars from other short-period variable stars without using the CMD needs to be developed, e.g., the distribution of δ Sct stars in the period–amplitude diagram (J. Lin et al. 2023a).

To test WFST's capability in searching for and detecting short-period variable stars, 20.5 minute UCB J0526+5934 (A. Kosakowski et al. 2023; J. Lin et al. 2024; A. Rebassa-Mansergas et al. 2024) was set as the targeted star of observations GP-20230918 and GP-20231116. As panel (b) of Figure 10 shows, despite a long dead time (≈30 s) of the camera, WFST can clearly reproduce the light curve for a 17.6 mag source having a variation period as short as 10.3 minutes (i.e., half of its orbital period). An outstanding feature is that its two minima within an orbit are distinguishable in the WFST phase-folded light curve (panel (f) of Figure 10), which supports the asymmetric geometry between two ends of the tidally distorted visible component. Such a feature from J0526+5934 has not been previously revealed by ZTF (A. Kosakowski et al. 2023), the Lijiang 2.4 m Telescope (J. Lin et al. 2024), or the 2.4 m Thai National Telescope (A. Rebassa-Mansergas et al. 2024).

One of the darkest ZZ Cet variables yet discovered. ZZ Cet variables are a type of pulsating WDs with almost pure

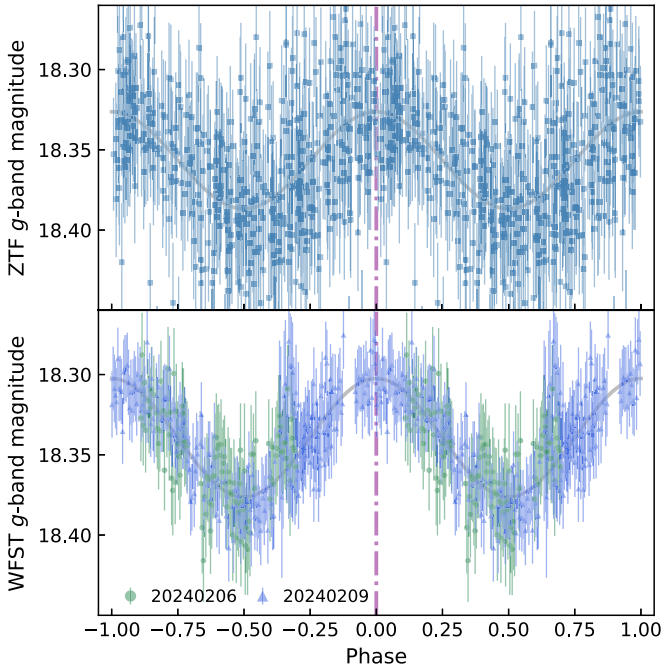

Figure 9. Phase-folded light curves of J0446+7219 provided by ZTF DR22 (upper panel) and WFST minute-cadence observations (lower panel). Both light curves are folded by the photometric period ($P = 2.95126$ hr) derived from the 6 yr ZTF g-band observations. For an ellipsoidal binary, its orbital period is twice the photometric period. The gray solid lines represent the best-fit sinusoidal models.

hydrogen atmospheres. Thanks to the densely sampled data from the Transiting Exoplanet Survey Satellite (TESS; G. R. Ricker et al. 2015), dozens of bright ($V < 16$) ZZ Cet variables have been discovered (A. D. Romero et al. 2022, 2024). However, due to rapid and relatively weak light variations, only a few ZZ Cet variables darker than 19 mag have been identified (S. Greiss et al. 2016). As introduced in Section 3.3.1, a significant 6.7 minute periodic signal from J0530+5945 was revealed (see also panels (c) and (g) of Figure 10). Given the minute-level periodic source located exactly within the instability strip of ZZ Cet (Figure 7), we identified this object as a new member of ZZ Cet variables. Benefiting from the high detection sensitivity and accumulating (daily-cadence/minute-cadence) observational data, a large number of ZZ Cet variables will be discovered by WFST, offsetting the absence of dark pulsating WDs in current survey missions.

Unspecific variable hot WD. J044659.23+722743.3 ($\alpha = 71.7468$ and $\delta = 72.4620$, hereafter J0446+7227) is one of the bluest stars among the stars covered by our minute-cadence observations. The color $(B_P - R_P)_0 = -0.58$ and absolute magnitude $G_{abs} = 10.89$ mag imply that J0446+7227 is a hot WD. By interpolating the synthetic photometry tables provided by MESA Isochrones & Stellar Tracks (MIST; J. Choi et al. 2016; A. Dotter 2016), this color corresponds to an effective temperature as high as 100,000 K. Within the observation GP-20240209, 25.3 minute periodic variations from this hot WD were marginally revealed (see Section 3.3.1). Additionally, the phase-folded light curve obtained from the observation GP-20240206 agrees with the periodic variations (panel (h) of Figure 10). Since its peak-to-peak amplitude is only 0.03 mag, which is comparable with WFST's photometric uncertainties at 18.3 mag, it is challenging for other survey missions to double-check the periodicity. As a hot WD with a (possible) variation period of about 25 minutes, J0446+7227 is inferred to be a candidate variable DO WD (DOV; A. H. Córsico et al. 2019) or rapidly rotating magnetic WD (L. Ferrario et al. 1997; I. Caiazzo et al. 2021). Further spectroscopic and high-precision photometric observations could provide crucial clues to classify the object.

4.3. Flaring Stars

Although dozens of time-domain survey missions are currently operating, only a few of them (e.g., TESS) are routinely performing observations in minute cadences, leading to a deficiency of stellar flares having dense observational sampling. Based on the minute-cadence observations of WFST, we present several well-sampled examples of stellar flares, ranging from 14 to 22 mag, in Figure 11. In the figure, four "energetic" flares, J053104.33+602810.3 (panel (d)), J053503.08+593657.0 (panel (e)), J044219.07+723213.1 (panel (g)), and J052843.23+585005.3 (panel (h)), were picked out by their high variabilities ($1/\eta$) rather than by Osten's method. Benefiting from the dense sampling rates, these flaring stars exhibit clear light-curve profiles during flares, allowing us to identify and describe the temporal morphologies of the flares (J. R. A. Davenport et al. 2014; W. S. Howard & M. A. MacGregor 2022), such as multiple peaks (panel (e) of Figure 11) and a highly impulsive peak followed by a "bump" (i.e., a peak–bump, panel (g)). The minute-cadence observations also revealed a short precursor emission prior to a large flare (panel (g)), and a slowly rising flare with a temporal structure that deviated from the typical impulsive profile (panel (d)). Interestingly, a fast, large-amplitude flare was emitted from a very faint M dwarf J052843.23+585005.3 (panel (h)). Its 22 mag quiescence magnitude is challenging to detect with current time-domain survey missions, and thus such a drastic flaring event could be incorrectly identified as an unknown fast optical transient.

A minute-timescale flare emerged from a very dark WD binary candidate. J042754.58+703423.2 ($\alpha = 66.9774$ and $\delta = 70.5731$, hereafter J0427+7034) is a very faint object located below the red end of the main sequence in the CMD (see Figure 7). Since its color $(B_P - R_P)_0 = 2.91$ and absolute magnitude $G_{abs} = 13.51$ mag overlap on the evolutionary tracks of WD–MS binaries (A. Rebassa-Mansergas et al. 2021), J0427+7034 is likely a binary consisting of a very dark WD and an M dwarf companion although the potential periodic light variations generated by its orbital motion are not detected. From this object, a fast flare lasting for only a few minutes was occasionally captured by WFST (see panel (a) of Figure 12). In order to confirm the abrupt light variation, we visually checked its images exposed before, on, and after the flaring event: the source was almost invisible before the event (panel (b)), then it significantly became bright within a minute (panel (c)) and decayed gradually (panel (d)). Such a transient flaring event from a 22 mag source is almost impossible to capture with other survey instruments. In the binary system of a WD+M dwarf, optical flares are likely induced by the chromospheric activity of the M dwarf or by accretion along the magnetic field lines of the WD (I. Pelisoli et al. 2023).

5. Summary

During the commissioning and pilot observation phases, we executed WFST minute-cadence observations on three different fields of the Galactic plane, with a total on-source time of about 13 hr. The accumulated fractions for the position deviations

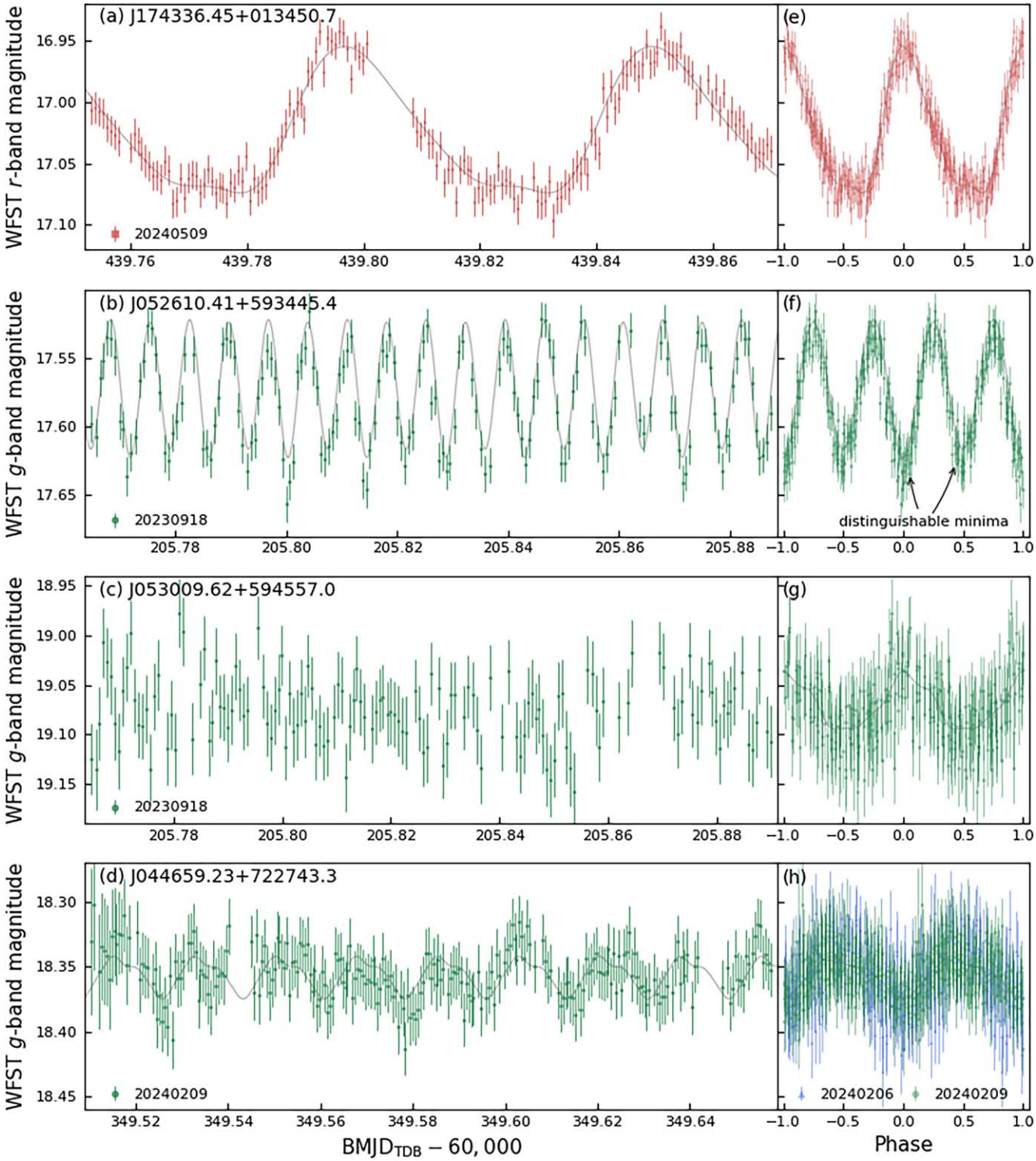

Figure 10. Uninterrupted light curves (panels (a)–(d)) and phase-folded light curves (panels (e)–(h)) for four short-period variable stars selected from WFST minute-cadence observations. These objects are 1.3 hr δ Sct star J1743+0134 (panels (a) and (e)), 20.5 minute UCB J0526+5934 (panels (b) and (f)), 6.7 minute ZZ Cet variable J0530+5945 (panels (c) and (g)), and 25.3 minute unspecific variable hot WD J0530+5945 (panels (d) and (h)). To double-check the periodicity, we present the phase-folded light curves for J0530+5945 obtained from two nights (panel (h)). The gray solid lines represent the best-fit fourth-order Fourier series.

suggest that WFST's astrometric precision is better than $0\farcs16$ for 90% of the astrometric measurements in these observations. By crossmatching all photometric measurements within a radius of $1''$, 650,696 uninterrupted light curves having at least 20 epochs, corresponding to 500,460 unrepeated WFST sources, were extracted from our observation data.

Via screening variable sources with variability index of $1/\eta$ and visually checking selected light curves, we found that about 0.1% of observed sources exhibit real astrophysical variability. In order to select light curves covering fast-flaring events, 486 flaring star candidates were selected from the uninterrupted light curves (with epochs $\geqslant 50$) through Osten's method, but only 33

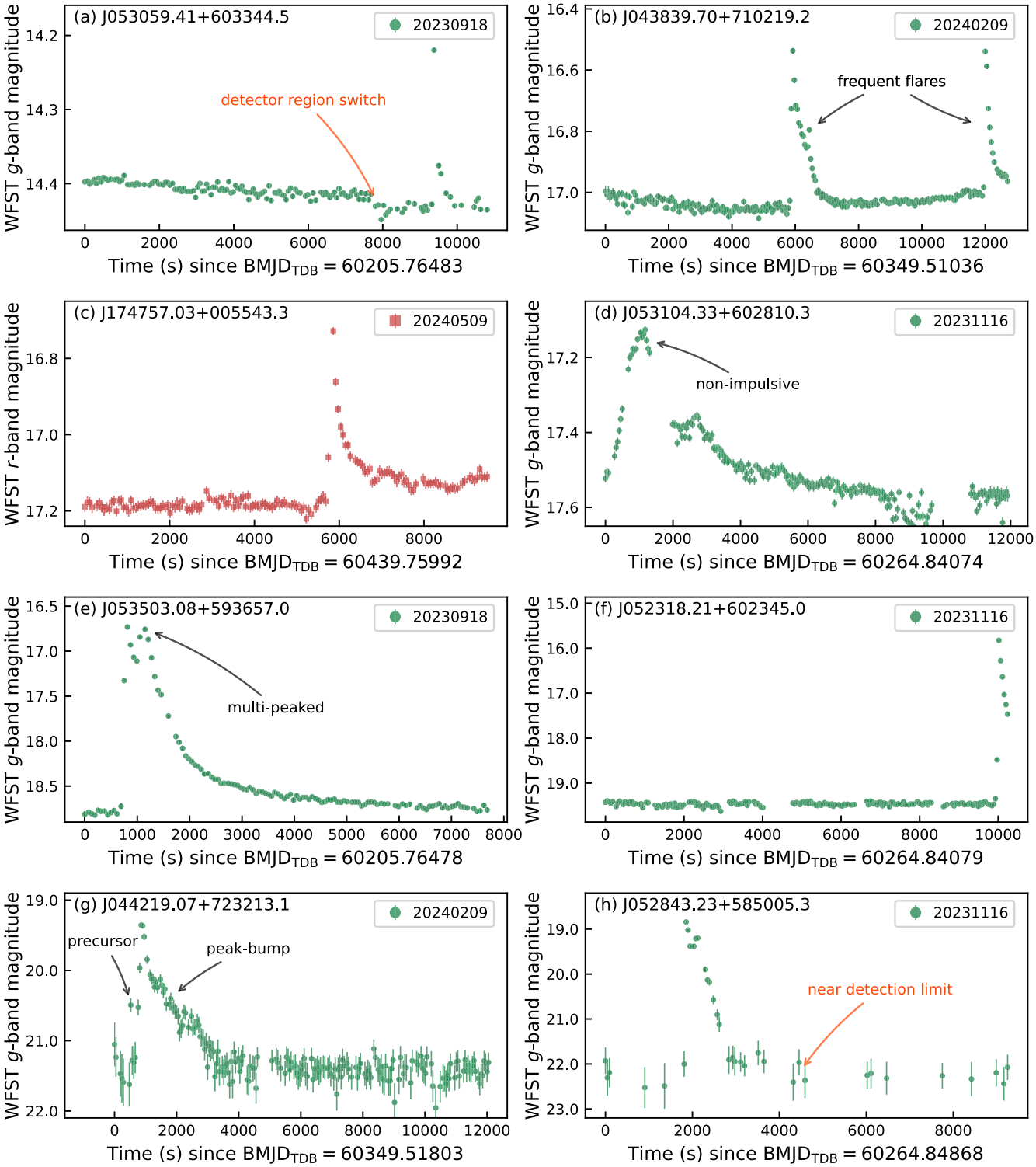

Figure 11. Uninterrupted light curves for eight flaring stars selected from WFST minute-cadence observations. All flaring stars are sorted by their quiescent magnitudes. We annotate the light-curve morphology for the flares (black arrows) as well as the observation issues (red arrows). Notice that, since each (4608 × 4616 pixel) region on the CCDs is processed separately in current pipelines, the bright sources switching among multiple detector regions could produce tiny systematic shifts in their light curves (see panel (a)).

ones show real flares by visual checking. Additionally, four flaring stars exhibiting "energetic" flaring events were discovered from the variable star candidates with significantly high $1/\eta$ values. By calculating the LSP for the uninterrupted light curves (with epochs $\geqslant$50) and plotting the $\mathrm{Pwr}_{\max}$–$f_{\max}$ diagrams, 10 short-period variable stars (with periods from several minutes to tens of minutes) were picked out. Additionally, 146 general periodic variable stars (with periods longer than 2 hr) were selected from splicing observations GP-20230918+GP-20231116 and GP-20240206+GP-20240209.

By crossmatching 500,460 WFST sources with the Gaia DR3 catalog, we found that 97.87% of them have at least a

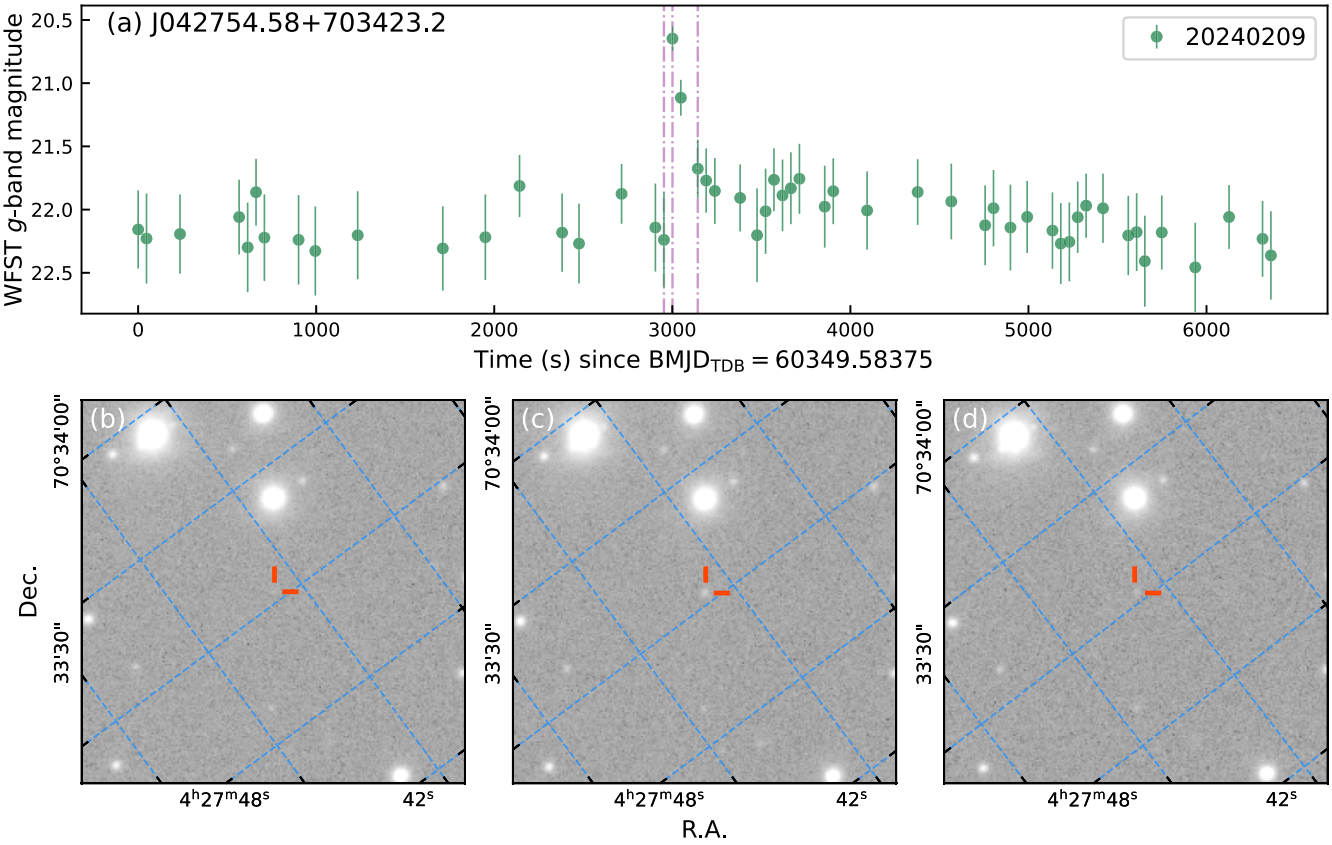

Figure 12. Uninterrupted light curve and finding charts for flaring star J0427+7034. The purple dotted–dashed lines overlaid on the light curve (panel (a)) indicate the epochs corresponding to the finding charts (panels (b)–(d)) in sequence. The red bars indicate the position of J0427+7034 in the images. The size of each image is 300 pixels × 300 pixels.

Gaia counterpart, and 20.93% of these Gaia sources have a reliable parallax measurement, which support determining their positions in the CMD. Referring to the catalog of WDs from Gaia EDR3 (N. P. Gentile Fusillo et al. 2021), there are at least 263 WD candidates covered by the WFST observations.

We presented the WFST light curves for a few periodic variable stars and flaring stars picked from our minute-cadence observations, and tried to identify the selected variable sources via their positions in the CMD (Figure 7). Besides the dominant EW-type eclipsing binaries and pulsating stars (e.g., RR Lyrae variables) among the selected general periodic variable stars, a 5.9 hr ellipsoidal binary candidate consisting of a WD and a low-mass MS star was first discovered from our observation data. The selected short-period variable stars include a few δ Sct stars, a known UCB (the targeted star of this field), a newly discovered and very faint ZZ Cet variable, and an unspecific variable hot WD. Furthermore, our minute-cadence observations captured flaring stars from 14 to 22.3 mag, covering diverse flare temporal structures, such as multipeaked and peak–bump flares. We also highlighted a minute-timescale flare that emerged from a candidate WD binary, while it is challenging for current survey missions to capture such a fast flare from a 22 mag star.

In conclusion, benefiting from its large aperture and thus deep detection limit, WFST can efficiently detect and reveal short-period variable stars and fast-flaring stars in unexplored parameter spaces, thus leading to new opportunities in discovering unique variable sources in the Northern sky. Following the commencement of regular survey operations, we will perform a systematic analysis of WFST observation data sets and publish comprehensive catalogs for detected variable stars.

Acknowledgments

We thank the anonymous referee for providing insightful comments. WFST is a joint facility of the University of Science and Technology of China and Purple Mountain Observatory. This work is supported by the National Key Research and Development Program of China (2023YFA1608100). J.L. is supported by the National Natural Science Foundation of China (NSFC; grant No. 12403038), the Fundamental Research Funds for the Central Universities (grant No. WK2030000089), and the Cyrus Chun Ying Tang Foundations.

ORCID iDs

Jie Lin https://orcid.org/0000-0003-3965-6931
Tinggui Wang https://orcid.org/0000-0002-1517-6792
Minxuan Cai https://orcid.org/0000-0003-4721-6477
Xuzhi Li https://orcid.org/0000-0002-2783-2080
Lulu Fan https://orcid.org/0000-0003-4200-4432
Qingfeng Zhu https://orcid.org/0000-0003-0694-8946
Ji-an Jiang https://orcid.org/0000-0002-9092-0593
Ning Jiang https://orcid.org/0000-0002-7152-3621
Xu Kong https://orcid.org/0000-0002-7660-2273
Zheyu Lin https://orcid.org/0000-0003-4959-1625
Jiazheng Zhu https://orcid.org/0000-0003-3824-9496
Wei Liu https://orcid.org/0000-0002-1490-5172

Yongquan Xue https://orcid.org/0000-0002-1935-8104
Wen Zhao https://orcid.org/0000-0002-1330-2329
Xianzhong Zheng https://orcid.org/0000-0003-3728-9912

References

Abramowitz, M., & Stegun, I. A. 1972, Handbook of Mathematical Functions (New York: Dover),
Aizawa, M., Kawana, K., Kashiyama, K., et al. 2022, PASJ, 74, 1069
Amaro-Seoane, P., Andrews, J., Arca Sedda, M., et al. 2023, LRR, 26, 2
Amaro-Seoane, P., Audley, H., Babak, S., et al. 2017, arXiv:1702.00786
Argiroffi, C., Reale, F., Drake, J. J., et al. 2019, NatAs, 3, 742
Bellm, E. C., Kulkarni, S. R., Graham, M. J., et al. 2019, PASP, 131, 018002
Borowicz, J., Pietrukowicz, P., Mróz, P., et al. 2023a, AcA, 73, 1
Borowicz, J., Pietrukowicz, P., Skowron, J., et al. 2023b, AcA, 73, 265
Burdge, K. B., Coughlin, M. W., Fuller, J., et al. 2019, Natur, 571, 528
Burdge, K. B., El-Badry, K., Marsh, T. R., et al. 2022a, Natur, 610, 467
Burdge, K. B., Marsh, T. R., Fuller, J., et al. 2022b, Natur, 605, 41
Burdge, K. B., Prince, T. A., Fuller, J., et al. 2020, ApJ, 905, 32
Byrne, C. M., & Jeffery, C. S. 2018, MNRAS, 481, 3810
Byrne, C. M., & Jeffery, C. S. 2020, MNRAS, 492, 232
Byrne, C. M., Stanway, E. R., & Eldridge, J. J. 2021, MNRAS, 507, 621
Cai, M., Xu, Z., Fan, L., et al. 2025, arXiv:2501.15018
Caiazzo, I., Burdge, K. B., Fuller, J., et al. 2021, Natur, 595, 39
Chambers, K. C., Magnier, E. A., Metcalfe, N., et al. 2016, arXiv:1612.05560
Chang, S.-W., Wolf, C., Onken, C. A., & Bessell, M. S. 2024, MNRAS, 529, 1414
Choi, J., Dotter, A., Conroy, C., et al. 2016, ApJ, 823, 102
Córsico, A. H., Althaus, L. G., Miller Bertolami, M. M., & Kepler, S. O. 2019, A&ARv, 27, 7
Coughlin, M. W., Burdge, K., Duev, D. A., et al. 2021, MNRAS, 505, 2954
Davenport, J. R. A., Hawley, S. L., Hebb, L., et al. 2014, ApJ, 797, 122
Deng, L., Yang, F., Chen, X., et al. 2021, Natur, 596, 353
Dotter, A. 2016, ApJS, 222, 8
Feng, F. B., Rui, Y. C., Du, Z. M., et al. 2024, AcASn, 65, 34
Feng, Q., Wang, H., Zhang, H.-f., et al. 2024, Proc. SPIE, 13096, 130963V
Ferrario, L., Vennes, S., Wickramasinghe, D. T., Bailey, J. A., & Christian, D. J. 1997, MNRAS, 292, 205
Finch, E., Bartolucci, G., Chucherko, D., et al. 2023, MNRAS, 522, 5358
Flewelling, H. A., Magnier, E. A., Chambers, K. C., et al. 2020, ApJS, 251, 7
Fukugita, M., Ichikawa, T., Gunn, J. E., et al. 1996, AJ, 111, 1748
Gaia Collaboration, Prusti, T., de Bruijne, J. H. J., et al. 2016, A&A, 595, A1
Gaia Collaboration, Vallenari, A., Brown, A. G. A., et al. 2023, A&A, 674, A1
Geier, S., Marsh, T. R., Wang, B., et al. 2013, A&A, 554, A54
Geng, Z., Wang, Z.-y., Zheng, Z.-h., et al. 2024, Proc. SPIE, 13101, 131010K
Gentile Fusillo, N. P., Tremblay, P. E., Cukanovaite, E., et al. 2021, MNRAS, 508, 3877
Green, G. M. 2018, JOSS, 3, 695
Green, G. M., Schlafly, E., Zucker, C., Speagle, J. S., & Finkbeiner, D. 2019, ApJ, 887, 93
Greiss, S., Hermes, J. J., Gänsicke, B. T., et al. 2016, MNRAS, 457, 2855
Güdel, M., Audard, M., Skinner, S. L., & Horvath, M. I. 2002, ApJL, 580, L73
Günther, M. N., Zhan, Z., Seager, S., et al. 2020, AJ, 159, 60
Guo, F., Lin, J., Wang, X., et al. 2024, MNRAS, 528, 6997
Hils, D., Bender, P. L., & Webbink, R. F. 1990, ApJ, 360, 75
Howard, W. S., & MacGregor, M. A. 2022, ApJ, 926, 204
Huang, S., Jiang, N., Zhu, J., et al. 2024, ApJL, 964, L22
Huang, S.-J., Hu, Y.-M., Korol, V., et al. 2020, PhRvD, 102, 063021
Jurić, M., Kantor, J., Lim, K. T., et al. 2017, in ASP Conf. Ser. 512, Astronomical Data Analysis Software and Systems XXV, ed. N. P. F. Lorente, K. Shortridge, & R. Wayth (San Francisco, CA: ASP), 279
Korol, V., Hallakoun, N., Toonen, S., & Karnesis, N. 2022, MNRAS, 511, 5936
Kosakowski, A., Kupfer, T., Bergeron, P., & Littenberg, T. B. 2023, ApJ, 959, 114
Kupfer, T., Bauer, E. B., Burdge, K. B., et al. 2019, ApJL, 878, L35
Kupfer, T., Bauer, E. B., Burdge, K. B., et al. 2020a, ApJL, 898, L25
Kupfer, T., Bauer, E. B., Marsh, T. R., et al. 2020b, ApJ, 891, 45
Kupfer, T., Korol, V., Littenberg, T. B., et al. 2024, ApJ, 963, 100
Kupfer, T., Korol, V., Shah, S., et al. 2018, MNRAS, 480, 302
Kupfer, T., Prince, T. A., van Roestel, J., et al. 2021, MNRAS, 505, 1254
Lamberts, A., Blunt, S., Littenberg, T. B., et al. 2019, MNRAS, 490, 5888
Lei, L., Zhu, Q.-F., Kong, X., et al. 2023, RAA, 23, 035013
Lin, J., Wang, X., Mo, J., et al. 2022, MNRAS, 509, 2362
Lin, J., Wang, X., Mo, J., et al. 2023a, MNRAS, 523, 2172
Lin, J., Wu, C., Wang, X., et al. 2023b, NatAs, 7, 223
Lin, J., Wu, C., Xiong, H., et al. 2024, NatAs, 8, 491
Lin, J., & Yu, W. 2018, MNRAS, 474, 1922
Lin, Z., Jiang, N., & Kong, X. 2022, MNRAS, 513, 2422
Liu, Q., Lin, J., Wang, X., et al. 2023, MNRAS, 523, 2193
Liu, Q., Lin, J., Wang, X., et al. 2024, Univ, 10, 337
Liu, Z.-Y., Lin, Z.-Y., Yu, J.-M., et al. 2023, ApJ, 947, 59
Lomb, N. R. 1976, Ap&SS, 39, 447
Lou, Z., Liang, M., Yao, D., et al. 2016, Proc. SPIE, 10154, 101542A
Lu, J.-Q., Fan, L.-L., Cai, M.-X., et al. 2025, PASP, 137, 024401
Macfarlane, S. A., Toma, R., Ramsay, G., et al. 2015, MNRAS, 454, 507
Magnier, E. A., Schlafly, E. F., Finkbeiner, D. P., et al. 2020, ApJS, 251, 6
Masci, F. J., Laher, R. R., Rusholme, B., et al. 2019, PASP, 131, 018003
McWhirter, P. R., & Lam, M. C. 2022, MNRAS, 511, 4971
Meng, X.-C., Han, Z.-W., Podsiadlowski, P., & Li, J. 2020, ApJ, 903, 100
Murphy, S. J., Hey, D., Van Reeth, T., & Bedding, T. R. 2019, MNRAS, 485, 2380
Murphy, T., Chatterjee, S., Kaplan, D. L., et al. 2013, PASA, 30, e006
Murphy, T., Kaplan, D. L., Stewart, A. J., et al. 2021, PASA, 38, e054
Nelemans, G., Yungelson, L. R., & Portegies Zwart, S. F. 2001, A&A, 375, 890
Ofek, E. O., Soumagnac, M., Nir, G., et al. 2020, MNRAS, 499, 5782
Osten, R. A., Kowalski, A., Sahu, K., & Hawley, S. L. 2012, ApJ, 754, 4
Pelisoli, I., Marsh, T. R., Buckley, D. A. H., et al. 2023, NatAs, 7, 931
Pietrukowicz, P., Dziembowski, W. A., Latour, M., et al. 2017, NatAs, 1, 0166
Pigulski, A., Kotysz, K., & Kołaczek-Szymański, P. A. 2022, A&A, 663, A62
Rappaport, S., Joss, P. C., & Webbink, R. F. 1982, ApJ, 254, 616
Rebassa-Mansergas, A., Hollands, M., Parsons, S. G., et al. 2024, A&A, 686, A221
Rebassa-Mansergas, A., Solano, E., Jiménez-Esteban, F. M., et al. 2021, MNRAS, 506, 5201
Reid, H. A. S., Vilmer, N., & Kontar, E. P. 2014, A&A, 567, A85
Ren, L., Li, C., Ma, B., et al. 2023, ApJS, 264, 39
Ricker, G. R., Winn, J. N., Vanderspek, R., et al. 2015, JATIS, 1, 014003
Romero, A. D., Kepler, S. O., Hermes, J. J., et al. 2022, MNRAS, 511, 1574
Romero, A. D., Kepler, S. O., Oliveira da Rosa, G., & Hermes, J. J. 2024, arXiv:2407.07260
Ruiter, A. J., Belczynski, K., Benacquista, M., Larson, S. L., & Williams, G. 2010, ApJ, 717, 1006
Scargle, J. D. 1982, ApJ, 263, 835
Sokolovsky, K. V., Gavras, P., Karampelas, A., et al. 2017, MNRAS, 464, 274
Toma, R., Ramsay, G., Macfarlane, S., et al. 2016, MNRAS, 463, 1099
VanderPlas, J. T. 2018, ApJS, 236, 16
Wan, Z., Fan, L., Li, X., et al. 2025, arXiv:2503.05160
Wang, B., Chen, W.-C., Liu, D.-D., et al. 2021, MNRAS, 506, 4654
Wang, S.-H., Fu, B.-X., Lu, J.-Q., et al. 2025, arXiv:2501.17472
Wang, T., Liu, G., Cai, Z., et al. 2023a, SCPMA, 66, 109512
Wang, Y., Murphy, T., Lenc, E., et al. 2023b, MNRAS, 523, 5661
Watson, C. L., Henden, A. A., & Price, A. 2006, SASS, 25, 47
Williams, K. A., Hermes, J. J., & Vanderbosch, Z. P. 2022, AJ, 164, 131
Wu, T., & Li, Y. 2018, MNRAS, 478, 3871
Xiong, H., Casagrande, L., Chen, X., et al. 2022, A&A, 668, A112
Yang, H., Liu, J., Qiao, E., et al. 2018, ApJ, 859, 87
York, D. G., Adelman, J., Anderson, J. E. J., et al. 2000, AJ, 120, 1579
Zhang, H.-f., Feng, Q., Wang, J., et al. 2024, Proc. SPIE, 13103, 131030V
Zhang, J.-C., Wang, X.-F., Mo, J., et al. 2020, PASP, 132, 125001
Zhu, Z.-y., Cao, Z.-h., Sun, Y.-c., et al. 2024, Proc. SPIE, 13098, 1309810